*Int. J. Electrochem. Sci.*, 11 **(2016)** 4966 – 4978, doi: 10.20964/2016.06.17

International Journal of
ELECTROCHEMICAL
SCIENCE
www.electrochemsci.org

# Single Phase $FeS_2$ (pyrite) Thin Films Prepared by Combined Electrodeposition and Hydrothermal Low Temperature Techniques

*R. Henríquez*[1,*], *C. Vasquez*[1], *N. Briones*[1], *E. Muñoz*[1], *P. Leyton*[1], *E.A. Dalchiele*[2]

[1] Instituto de Química, Facultad de Ciencias, Pontificia Universidad Católica de Valparaíso, Av. Universidad 330, Curauma, Valparaíso, Chile.
[2] Instituto de Física & CINQUIFIMA, Facultad de Ingeniería, Julio Herrera y Reissig 565, C.C. 30, 11000 Montevideo, Uruguay.
[*]E-mail: rodrigo.henriquez@pucv.cl

*Received:* 24 February 2016 / *Accepted:* 26 March 2016 / *Published:* 4 May 2016

In current work the synthesis of single phase of $FeS_2$ (pyrite) thin films from a combined electrochemical and hydrothermal techniques and without the need for a post sulfurization process is reported. Electrodeposition has been carried out in a non aqueous based electrolytic bath (diethylene glycol (DEG)). Voltamperometric measurements were conducted to study the electrochemical response of the precursors in this organic DEG solvent. These experiences allowed determining the best experimental conditions in DEG for obtaining the $FeS/FeS_2$ mixture phases which were obtained applying a constant potential of –1.10V. The hydrothermal technique that was developed in a microwave oven improved stoichiometry and crystallinity of the deposits obtained by electrodeposition and led to obtaining a single pyrite phase. SEM micrographs exhibited complete substrate coverage whereas EDS analysis gave atomic ratio S/Fe very close to 2. XRD analysis of the final thin film shows that the deposit has a cubic structure without the presence of other undesired phases. However, Raman spectra indicate a later formation of amorphous superficial hematite. The optical measurements show an optical direct bandgap of 0.985 eV. Results open the possibility of applying the procedure to the formation of a thin film of $FeS_2$ of good structural and optical characteristics that can be employed as an absorber material in solar cells.

**Keywords:** pyrite thin films, electrodeposition, hydrothermal, low temperature, semiconductor material.

## 1. INTRODUCTION

Direct conversion of solar energy into electricity by photovoltaic solar cells is one of the most important of the several approaches for solar energy utilization [1-3]. At the moment, one of the key

priorities in photovoltaic solar energy conversion domain is to lower the fabrication costs while maintaining high sunlight into electric power conversion efficiencies [4-6]. Then, further advancement in the research and development of new solar cells, i.e.: structures and device architectures, and new materials, focused on the use of cheap and non-toxic materials, prepared via cost-effective and low-temperature synthesis techniques is required to: i) increase the light to electric power conversion efficiencies, and ii) to reduce costs [3,7].

Generally speaking, materials selection for future photovoltaics should satisfy several important criteria. The materials should be comprised of abundant and inexpensive elements. The materials should be environmentally benign to avoid any issues of potential environmental contamination. And importantly for any potential photovoltaic application, the materials must have an optimal band gap to maximize solar absorption such that the resulting solar cell would have marketable energy conversion efficiency. In a recent published report, nine inorganic semiconductors were highlighted as having both the annual electricity production potential in excess of worldwide demand and material extraction costs cheaper than that of crystalline silicon [8]. Within them, iron disulfide, $FeS_2$ (pyrite) semiconductor compound has been individualized as the most attractive photovoltaic material for large-scale future deployment of efficient and low cost solar cells [8]. In fact, the development of pyrite as a solar energy material is motivated by its non-toxicity (environmentally green-alternative), by the abundance of its constituents (economical viable and earth-abundance) and by its opto-electronic properties [9,10]. However, and despite being a very promising semiconductor material for use as the active absorber layer in solar photovoltaic and photoelectrochemical cells, still remains under-researched [11].

Pyrite is a semiconductor material that can be *n* or *p* type depending on the impurity species present [12]. It has a suitable band gap (an indirect transition at 0.95 eV [13-15] and a direct one at 1.03 eV [13]), strong light absorption ($\alpha > 10^5$ $cm^{-1}$ for $h\nu > 1.3$ eV, two orders of magnitude greater than crystalline silicon) [15-17] and an adequate minority carrier diffusion length (100-1000 nm) [10,15,16]. The large absorption coefficient is particularly advantageous because only 40 nm of pyrite are required to absorb 90% of the incident light [7,17]. Pyrite photoelectrochemical and Schottky solar cells were first demonstrated by Tributsch in 1984 [11]. Pyrite devices show high quantum efficiencies (often >90%) and photocurrents (>40 mA $cm^{-2}$) but small photovoltages (typically <200 mV, ~20% of the band gap) [11], being this low photovoltage value responsible of the limited solar cell efficiency. In fact, pyrite based solar cells fabricated to date exhibit less than 3% conversion efficiency, even though theoretical analysis predicts that greater than 18% should be attainable [18]. The low photovoltage is attributed to both bulk and surface vacancies that generate electronic states within the band gap [11]. So, enhancing the photovoltage and efficiency of pyrite based solar cells requires basic research on the growth, surface passivation, and structural and electronic characterization of pyrite films [11]. Moreover, impure phases as FeS and $Fe_{1-x}S$ which have small band gaps (0.004 eV for FeS and 0.2 eV for $Fe_{1-x}S$), would affect the efficiency of photovoltaic devices [19]. Hence, to develop a synthesis process to fabricate a perfect stoichiometric $FeS_2$ is essential [19].

Pyrite thin films have been prepared by a variety of gas-phase methods [20], i.e.: sputtering and metal-organic chemical vapor deposition [18]; and solution-phase methods, i.e. spray pyrolysis, chemical bath deposition, electrophoretic deposition, sol-gel [20] and sulfurization of

electrochemically deposited Fe-S layers [21-25]. So far, the gas-phase preparation methods adopted are mostly at high temperatures [19]. Moreover, in the case of the solution-phase methods, the strategy adopted in most of these cases is to deposit a film of (often amorphous) iron oxides or iron sulfides, and anneal the film in sulfur gas at elevated temperatures (350-600 $^{o}$C) to produce polycrystalline pyrite [20]. However, segregation of iron and sulfur inevitably occurs at those elevated temperatures, which consequently deteriorates the quality of the obtained films [26]. In the particular case of the electrochemical route, to the best of our knowledge there are no papers reporting electrodeposition of single phase pyrite thin films in one step. In fact, in all those papers cited above, a hard high temperature sulfurization second step process was needed in order to obtain the desirable single pyrite phase [21-25]. Hence, one of the most important benefits of the electrodeposition (a low temperature process [27]) is lost. On the other hand, hydrothermal treatment appears as a low temperature alternative route to those hard annealing processes. Hydrothermal method both as a synthesis and a treatment method is the most attractive one due to its perfect control of morphology, purity, crystallinity, composition and low cost for large-scale production [28,29]. Moreover, hydrothermal treatment has been proved with respect to annealing, to be more effective and better to enhance the optoelectronic properties of electrodeposited semiconductor materials [28]. On the other hand, although the electrochemical reduction of elemental sulfur in nonaqueous media has been vastly and successfully used in the synthesis of different semiconductor materials (i.e.: CdS, CdS-CdSe mixture phases, etc. [30,31], to the best of our knowledge only one report concerning the formation of pyrite thin films from a non-aqueous electrolytic bath has been reported by Giornada et al. [32]. These authors reported that the as-grown films were amorphous and indicated the presence of some crystalline phase of $FeS_2$ and FeS after an annealing at 285°C [32].

In the present work, single phase pyrite thin films are prepared by combined electrodeposition from a non-aqueous based electrolytic bath and hydrothermal relatively low temperature techniques (below 160 $^{o}$C).

## 2. EXPERIMENTAL

$FeS_2$ thin films were prepared by combined electrochemical and hydrothermal techniques. The potentiodynamics and potentiostatics measurement were developed in a conventional three electrode electrochemical cell at 80°C in a Diethylene glycol (DEG) based solution containing a 5 mM of $FeSO_4 \cdot H_2O$ (SIGMA-ALDRICH 86.0-89.0%), 0.15 M of Thiourea (TU, MERCK 99.0%) and 0.1 M LiCl anhydrous (MERCK 99.9%) as supporting electrolyte. The working electrode substrates were glass plates coated with FTO ($SnO_2$:F), the counter electrode was a platinum wire (99.99%) and a $Ag/AgCl_{sat.}$ ($E° = +0.199$ V vs. NHE) was used as reference electrode. The working electrode were rinsed and subsequently cleaned in an ultrasonic bath with acetone and chemically treated in fresh 1 M nitric acid solution for 20 min at room temperature to improve the adherence of the electrodeposit. Electrochemical measurements were performed using a CH-Instrument electrochemical Analyzer model 604C connected to PC. Before each electrochemical experience, the solution was aerated for 30 minutes with high purity argon. The potentiostatics electrochemical synthesis of initial deposit was

carry out applying a constant potential of –1.10V for 30 minutes onto a clean FTO electrode of the geometric area 1.0 $cm^2$. The hydrothermal technique was developed in a microwave Milestone Start D model for three hours at 160°C. The solution composition of the hydrothermal treatment was obtained from bibliographic information where all relevant chemical aspects are explained [26].

Scanning electron microscopy (SEM) images and quantitative elemental analysis were obtained using a Jeol instrument JSM 6300 model and EDS Bruker Nano GmbH with XFlash Detector model 410M respectively. Atomic force Microscopy (AFM) images were obtained through the Nanoscope Digital model IIIa, disposed in Tapping mode at scan rate of 10 μm/s. X-ray diffraction spectra of thin films were recorded on an X-ray diffractometer, Bruker model D8 Advance, using a parallel beam in grazing incidence. In this configuration the angle of the incident beam remains constant ($\theta_i$) while the detector angle moves 2θ degrees. The parallel beam was obtained by passing the Cu-$K_\alpha$ ($\lambda$= 1.5406 Å) radiation of an X-ray tube. The samples were scanned from 2θ = 20 to 70º in steps of 0.02º at a speed of 1º/min. The Raman spectra were scanned with a Witec Alpha 300 confocal Raman microscope system equipped with 785 nm excitation laser wavelengths, and an electrically cooled CCD camera. The signal was calibrated by using the 520 $cm^{-1}$ line of a Si wafer and a 20x objective. The laser power on the samples was 2 mW. The resolution was set to 4 $cm^{-1}$ and 20 scans of 1 s integration time. Spectra were recorded in the 200 - 1800 $cm^{-1}$ region. All samples were photo stable when probed with 785 nm laser line. Optical properties as well as the optic bandgap were monitored by transmittance using UV-2600, UV-Vis Spectrophotometers between 1400 to 500 nm. The measurements of the optical properties were developed at room temperature. The samples were measured front of air and not FTO clean substrate was employed as reference.

## 3. RESULTS AND DISCUSSION

### *3.1 Electrochemical growth process of pyrite precursor thin films.*

First of all and before to carry out the electrochemical growth of the pyrite thin films, the electrochemical response of the precursors was studied in order to optimize the composition of the $Fe^{2+}$ and TU in the DEG based electrolytic solution. In this sense, the best results obtained in the potentiostatic electrochemical synthesis have been achieved by employing a concentration ratio of 1:30 between $Fe^{2+}$ and TU respectively. Figure 1 shows the potentiodynamics response of the $Fe^{2+}$/TU system. According to the potentiodynamics study of the single precursors and the literature information [33.40], the assignation of the different observed electrochemical processes are indicated.

In the cathodic sweep, the $Fe^{3+}$/ $Fe^{2+}$ couple reduction process can be observed at –0.04 V, that it is followed at more cathodic potentials by a process which can be located at –1.18 V. This process can be associated with the reduction of TU according to (1) [38-40]. Continuing the sweep, the formation of metallic iron phase ($Fe^{2+}$/ Fe° couple) can be observed over to –1.45 V. This latter process has a 0.20 V cathodic shift in comparison with the response of the metallic ion precursor. This displacement can be associated with the formation of a semiconducting phase due to the rapid precipitation process between $Fe^{2+}$ and the $S_x^{2-}$ ion previously formed from the electrochemical

reduction of TU (see reaction (2)). In the reverse scan, the TU to formamidine disulfide (FDS) oxidation process can be observed at –0.58 V (see reaction (3)).

The process labeled as $C_I$ that can be observed at –0.09 V can be assigned to the anodic stripping of the different pyritic solid phases (*ac*. $FeS_{1-x}$, $FeS_2$) to $Fe^{2+}$ and $S_x$. Finally, the last anodic process at +0.2V can be associated to the oxidation process of the $Fe^{2+}/Fe^{3+}$ couple. Thus, it can be concluded that the interest electrochemical processes to the eventual production of thin films of pyrite occur in the –1.00 V and –1.25 V potential ranges. However, the different synthesis performed in this potentiostatics potential range showed that the best results were obtained when the deposits were conducted by applying a constant potential of –1.10V. In present work, only these results are shown.

$$(NH_2)_2CS + 2e^- \rightarrow 2S^{2-} + CN^- + 2NH_4^+ \quad (1)$$

$$Fe^{2+} + S_x^{2-} \rightarrow FeS_x \quad (x = 1, 2) \quad (2)$$

$$2(NH_2)_2CS \quad (H_2N)_2(HN)_2C_2S_2 + 2H^+ + 2e^- \quad (3)$$

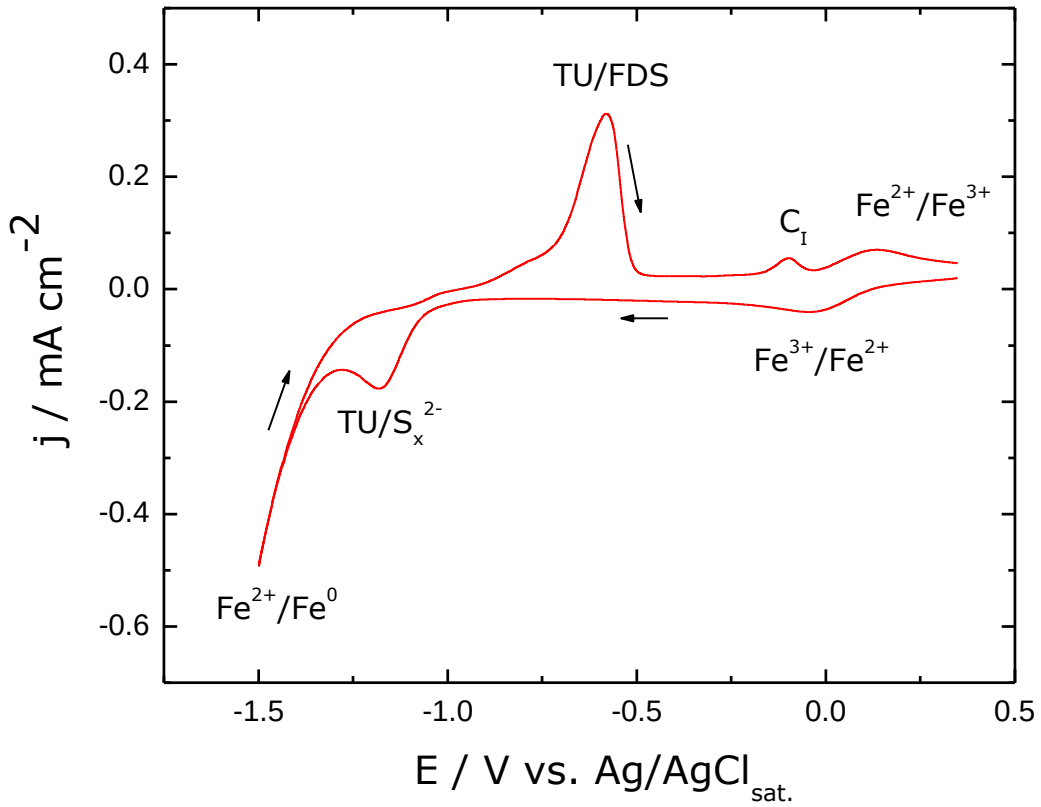


**Figure 1.** Third cycle of the potentiodynamic response obtained from the $Fe^{2+}$/TU system onto a FTO electrode in DEG solution at 80°C. The arrows indicate de directions of the scan recorded at $0.050 Vs^{-1}$.

*3.2 Structural, Morphological and optical characterization of the pyrite thin films.*

After the potentiostatic synthesis at –1.10 V and prior to the hydrothermal treatment, the as-grown thin films were homogenous and adherent, exhibiting a dark yellow-gray color film. Unfortunately, X-ray diffraction studies showed that these as-grown deposits were amorphous in nature. Moreover, after a simple annealing treatment at 350°C for 1 hour under an argon atmosphere, only a very slight improvement on the crystallinity of the films has been observed. In these samples, phases of FeS (troilite), $Fe_{1-x}S$ (pyrrhotite) and $FeS_2$ (pyrite) could be identified. Then, at the place of an annealing tretament an hydrothermal treatment was performed to the as-grown samples in order to improve both the crystallinity and stoichiometry of the deposits. After this procedure the films exhibited excellent adhesion and a dark gray color over the entire surface of electrode. Figure 2 shows an X-ray diffractogram pattern of a typical electrochemically grown pyrite precursor after the hydrothermal treatment. Excluding the diffraction peaks of the FTO ($SnO_2$) substrate, the remaining diffraction lines are related to polycrystalline cubic iron pyrite phase (cubic $FeS_2$, JCPDS #42-1340; a = 5.417 Å). In particular, very important is the presence of diffraction peak characterizing pyrite at 2θ = 56.23°, diffraction plane (311). No shift in the peak positions are measured between the experimental and JCPDS pattern in the whole angular range (20-70 degrees), and the ratios of their intensities correspond well to those from JCPDS file database, indicating that any significant prevailing orientation, often connected with internal tension of films, did not occur [41,42]. No other impurities phases such as hexagonal (FeS [JCPDS #65-9124]), marcasite ($FeS_2$, [JCPDS #74-1051]), pyrrhotite ($Fe_7S_8$ [JCPDS #29-0723]), greigite ($Fe_3S_4$ [JCPDS #16-0713], S or Fe-O compounds were detected, confirming the high purity of the pyrite films. Average crystallite size was calculated from a full width at half maximum (FWHM) of X-ray diffraction peaks by using Scherrer formula [43]. The average crystallite size calculated from (200) diffraction peak was 30 nm, showing that the films are nanostructured. On the other hand, as has been previously reported that the lattice constant of synthetic pyrite can vary from 5.428 to 5.407 Å, which is attributed to sulfur vacancies in pyrite (up to 13%, $FeS_{1.74}$) grown at high sulfidation temperatures (≥450 $^oC$) or prolonged annealing times, causing up to 1% lattice compression [17]; it should be very important to calculate the lattice constant from the X-ray diffraction patterns. Then, first, the lattice parameter of the cubic unit cell of the pyrite thin film has been calculated from the 2-theta peak positions in the X-ray diffraction patterns. After that and from the Nelson–Riley plots, the corrected value of lattice constant has been estimated. For this, the lattice parameters calculated from the 2-theta peak positions of individual reflections are plotted against $\cos^2\theta$ $(1/\sin\theta + 1/\theta)$ and the intercept of the linear plot at $\cos^2\theta$ $(1/\sin\theta + 1/\theta) = 0$ gives the lattice constant [44]. Figure 3 represents the plot of lattice constants (a) against $\cos^2\theta$ $(1/\sin\theta + 1/\theta)$ for a typical pyrite thin film. The estimated value of lattice parameter for the $FeS_2$ thin film is a = 5.416 Å. This value is close to the lattice parameters reported for $FeS_2$ (a = 5.417 Å [JCPDS #42-1340]), in agreement with an stoichiometric pyrite phase [17]

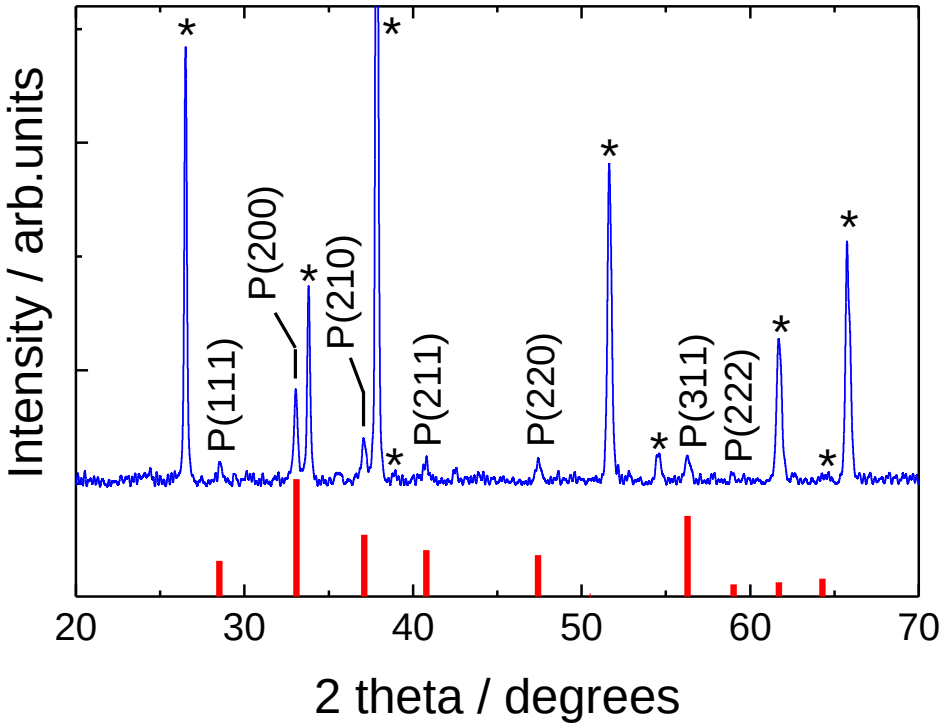


**Figure 2.** X-ray diffraction pattern of a pyrite thin film grown onto FTO substrate after hydrothermal treatment. Diffraction planes are indicated for $FeS_2$ (P(hkl)). Cubic pyrite JCPDS pattern is also shown for comparison ($FeS_2$ JCPDS: thick blue bars). (*, indicates the peaks originated from the $SnO_2$:F substrate).

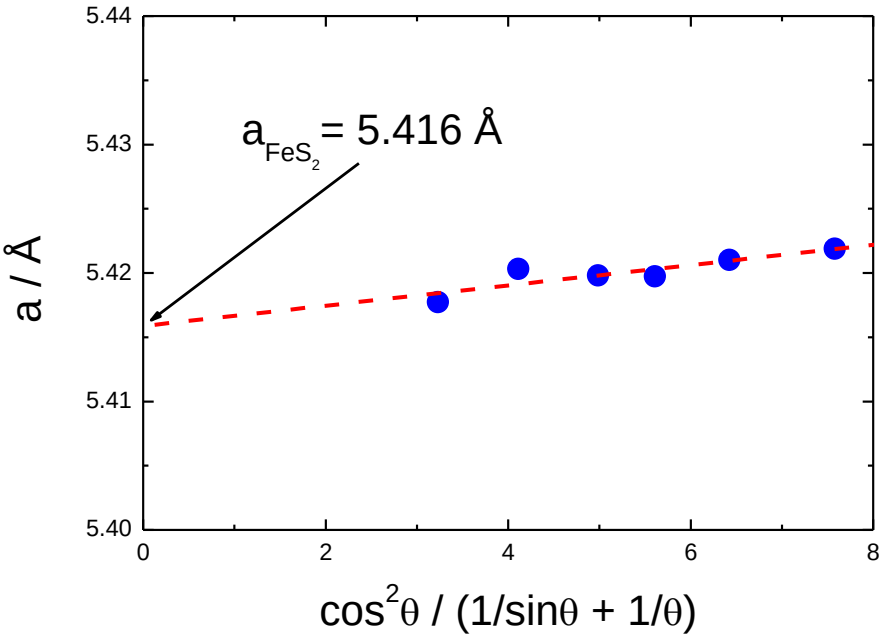


**Figure 3.** Nelson–Riley plot for a pyrite thin film grown onto FTO/glass substrate. The estimated value of lattice parameter for the pyrite film is also indicated.

Considering the lower impurity detection limits that has the XRD measurements [45], Raman spectroscopy was applied to further confirm the pure phase of pyrite thin films due to its capability to distinguish iron sulphide phases (such as FeS, $FeS_2$, and $Fe_3S_4$) that may have been present in the film [17,26]. Figure 4 shows the recorded spectra obtained for a pyrite thin film electrodeposited at –1.10 V and submitted to a post hydrothermal treatment. The figure shows three characteristic strong bands at 226.6 $cm^{-1}$, 295.3 $cm^{-1}$ and 410.6 $cm^{-1}$ assigned to hematite. Likewise, a second group of three signals are characterized by a shoulder at 307.6 $cm^{-1}$, followed by a strong band at 314.3 $cm^{-1}$ and other with a medium to weak intensity at 379.1 $cm^{-1}$ are coincident with the presence of pyrite in the deposit. The presence of hematite in the Raman spectrum can be explained by two approaches. The first, results from the hydrothermal process according to chemical reactions 4 and 5 respectively [26]. The second is related to the thermodynamic instability of the non-stoichiometric pyritic phases respect to iron oxide. In this sense, the chemical oxidation of these phases in the presence of atmospheric oxygen can lead to surface formation of hematite. From the above, the second approach seems more correct considering that hematite is not present in the XDR patterns indicating that is only superficial or present an amorphous structure.

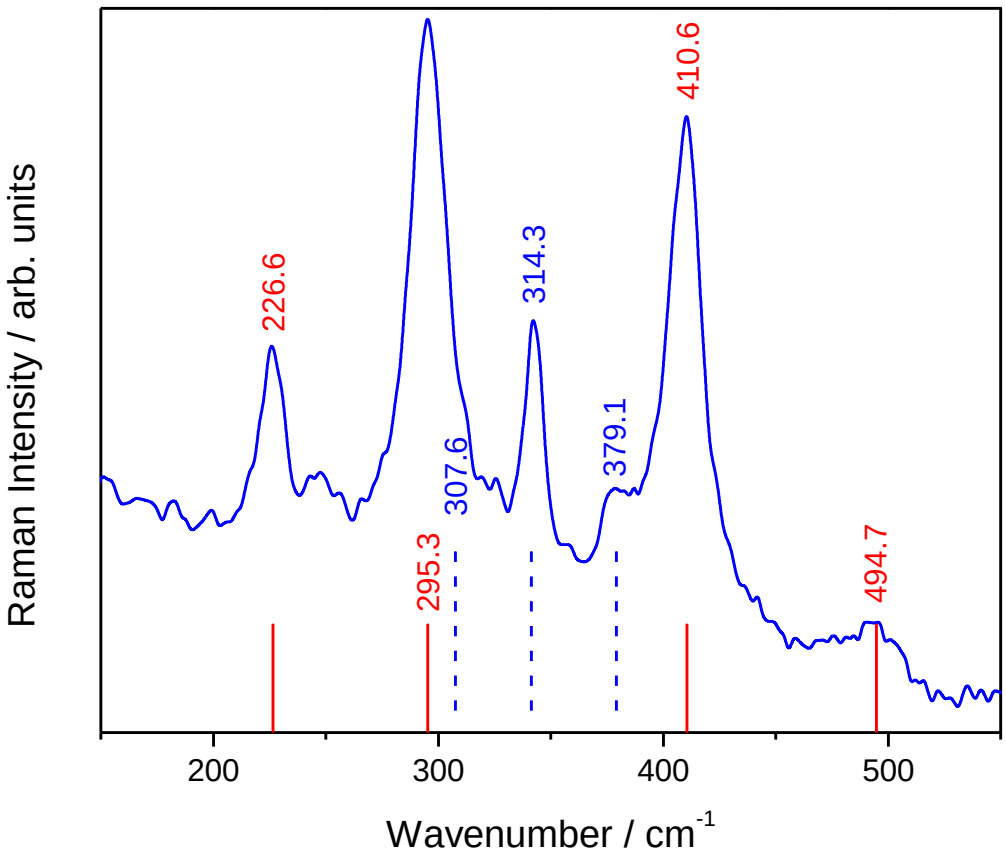


**Figure 4.** Typical Raman spectra of an electrodeposited pyrite sample after hydrothermal treatment with. For comparison Raman lines corresponding to: (—) hematite R0400 and (----) pyrite R100166 (both from RUFF database) are also depicted.

$$2Fe^{3+} + 3S^{2-} + 3H_2O \rightarrow 2Fe(OH)_3 + 3H_2S \quad (4)$$

$$2Fe(OH)_3 \rightarrow Fe_2O_3 + 3H_2O \quad (5)$$

While the characterization proved the presence of hematite, this method cannot be used to obtain the concentration of this phase due to the inherent disadvantages of Raman spectroscopy. For example, the illuminated area by excitation laser beam must be small (ac. 1$\mu m^2$ approximately) in order to provide appropriate signal to noise ratio. However, a narrow beam does not allow obtain spectrum over a significant area of the sample. Other important factors that deserve consideration are the frequency of laser used to excite the sample, the Raman cross section of the mineral and the relative orientation of the crystal relative to the direction of polarization of the laser. Moreover, in the case of samples with different particle size some experimental factors such as laser power, beam diameter and the angle of incidence on the surface sample also affect the intensity of the Raman signal. The effective sampling volume depends on both the depth and the illuminated area. Thus, the focus of the laser, the particle size of the mineral, the roughness of the sample and the optical phenomena related with the interface, such as reflections and refractions affect experimentally the Raman measurements. Because all these factors, the bands observed in the Raman spectra cannot be related to the concentration of the constituents. In this context, the minimum differential Raman cross section is in the order of $(d\sigma/d\Omega) \approx 10^{-31}$ - $10^{-28}$ $cm^2$ $sr^{-1}$. Accordingly, if the mineral concentration in the surface is in orders of magnitude comparable with a molecular monolayer within the sample volume, detection of the mineral would not be possible.

Figure 5 shows the SEM and AFM images obtained after hydrothermal treatment. As it can be seen in Fig. 5a, the deposit is compact, homogeneous on the substrate surface and has an irregular morphology. The presence of a combination of structures can also be found. Firstly, it can be seen the presence of the typical cauliflower type structure that is obtained in deposits formed through a precipitation reaction where one component is electrochemically formed (sulfide ion, see Eq. 1 and 2). Furthermore, it is also seen as the deposit has cubic structures distributed irregularly in the film surface. These cubic structures have been studied by AFM (see Fig. 5b). In fact, the average length of the edge considering the three axes has a value of 1.081 ± 0.005 μm confirming the cubic structure. On the other hand, the deposits show an average roughness means square (RMS) of 250.8 ± 70.0 nm and a roughness factor of 1.429 ± 0.200. These values demonstrate the high irregularity of the final deposit which is consistent with the small average grain size of 192.2 ± 81.9 $nm^2$ also can be obtained. Finally, the quantitative elemental analysis was be obtained by EDS. The general analysis of the surface of the film shows an atomic ratio $\%At_S/\%At_{Fe}$ = 1.89 and the 1.99 only when cubic structures are analyzed. Though atomic composition values are very close to the expected ideal value (*ac*. 2), they are good indicators of the possible presence of pyrite as single phase component of the deposit.

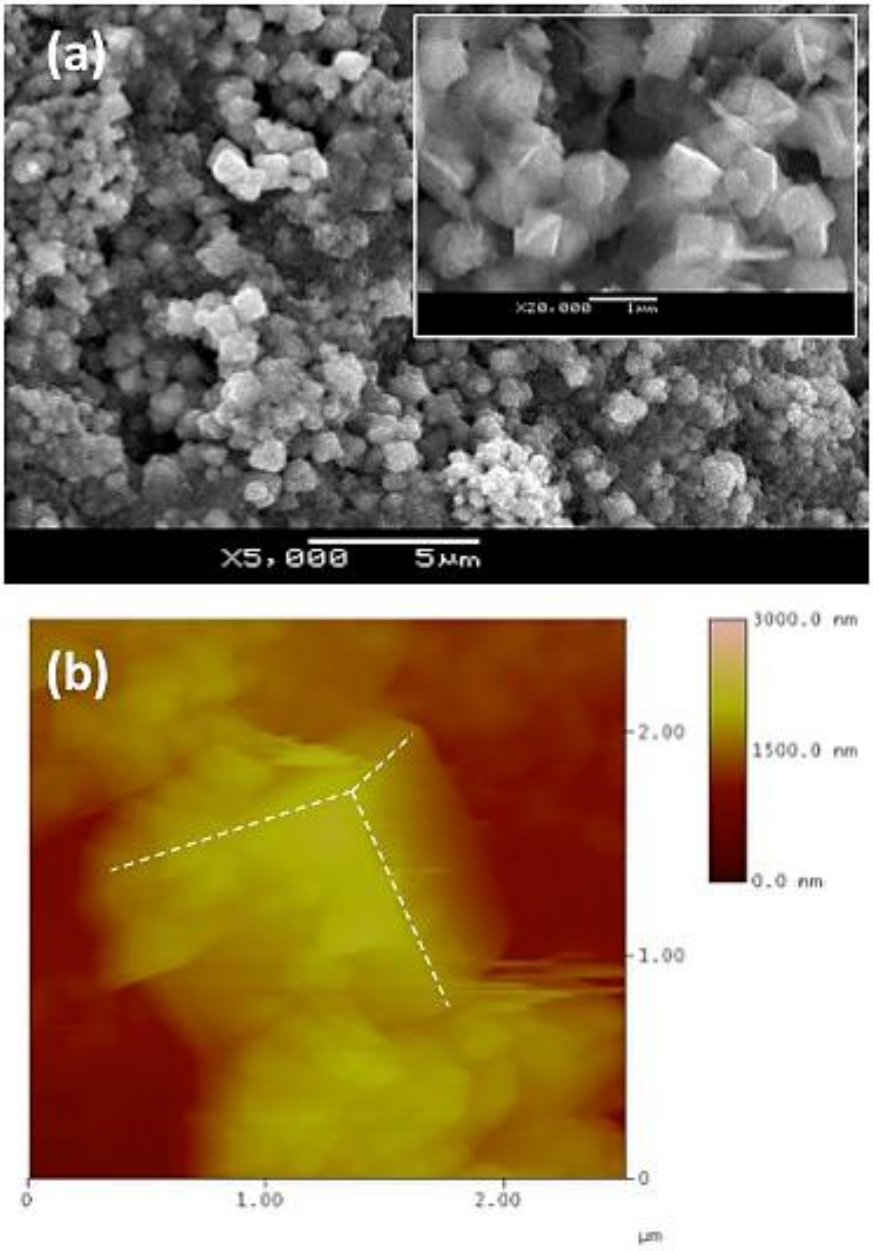


**Figure 5.** (a) SEM plan-view micrograph image of a pyrite thin film grown onto an FTO/glass substrate from a potentiostatics film formed –1.10 V and after the hydrothermal treatment. Inset shows a high magnification top view image of this pyrite layer revealing cubic prism shape of the grains. (b) Typical AFM image of a pyrite thin film. Dashed white lines are guide for the eye in order to reveal the cubic shape of a single pyrite grain.

Figure 6a shows the typical absorption spectra of an electrodeposited pyrite thin film obtained after hydrothermal treatment. This absorption coefficient α was obtained from a transmittance spectra by $\alpha = -(1/d) \ln T$ where "d" corresponds to the thickness of the deposit (reflectance and dispersion of light on the thin film and on the substrate were neglected). A thickness of d = 375 nm has been estimated through SEM cross-sectional image of a sample observing the pyrite/FTO interface. The pyrite layer exhibits a high optical absorption coefficient ($\alpha > 10^5$ $cm^{-1}$) in visible and near-infrared spectral regions. So, this pyrite films meet clearly one of the requirements for excellent solar absorber

material in solar cells. Moreover, the classic oscillatory behavior product of the interference waves from FTO substrate [37rr] can only be evident to short high energy wavelength. The presence of interference waves indicating the low thickness of the obtained pyrite film. As $FeS_2$ optical behavior is principally that of a direct semiconductor [46], it is expected that $\alpha \propto (h\nu - E_g)^2 / h\nu$ [47,48] where $h\nu$ is the photon energy and $E_g$ is the direct bandgap.

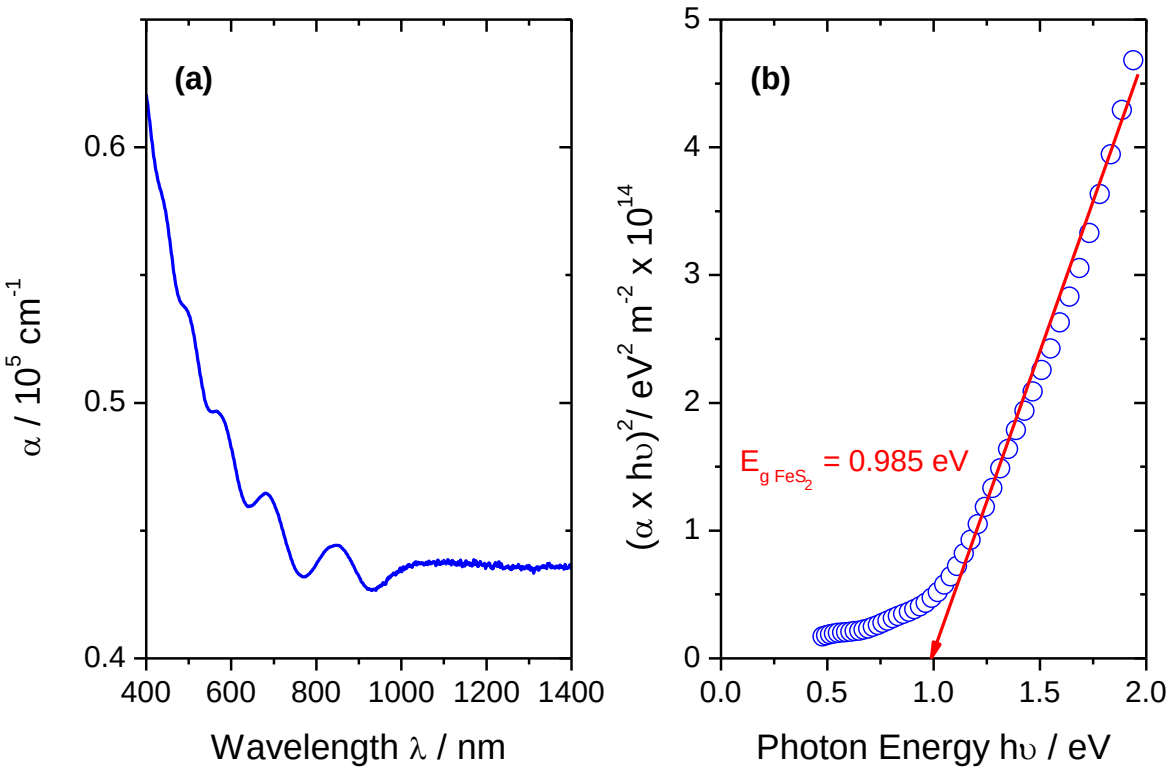


**Figure 6.** (a) Typical optical absorption spectra of and electrodeposited and hydrothermal treated pyrite thin film. (b) Direct bandgap energy estimation for this for pyrite sample: (o) $(\alpha \times h\nu)^2$ plots and (—) linear fittings for whole $FeS_2$/FTO/glass.

The bandgap energy can be obtained by a linear fitting of $(\alpha \times h\nu)^2$ vs $h\nu$ plot [49]. As shown in figure 6, it can be seen that the $(\alpha \times h\nu)^2$ vs $h\nu$ plot follows an almost linear dependence above the bandgap value and is almost zero below this value. This zero value validates the approximation previously done neglecting the reflectance and dispersion. For pyrite thin film obtained by electrodeposition with hydrothermal treatment, the bandgap energy has a value of 0.985 eV which it is very close to those values reported by other workers [13]. The small differences that can be found may be related to the presence of hematite surface observed through Raman spectra or the presence of other nonstoichiometric pyritic phases within the pyrite thin film. They can introduce interband energy levels that can lead to the decline in value of the optical bandgap of the synthesized samples [50]. Finally, indirect transitions of the film could not be obtained.

## 4. CONCLUSIONS

Pyrite thin films have been successively deposited onto FTO/glass substrates by combined electrochemical and hydrothermal low temperature techniques, and without the need for a post sulfurization process. X-ray diffraction analysis of the resulting thin film shows that the deposits exhibit a polycrystalline cubic iron pyrite phase, with a lattice parameter of 5.416 Å, in agreement with a stoichiometric pyrite phase. Homogeneous and well adherent pyrite thin films have been obtained, exhibiting a dark gray color to the naked eye. The synthesis method developed achieves the formation of the pyrite phase with a negligible amount of impurities that in turn does not significantly affect the value of bandgap of the pyrite phase. With a high optical absorption coefficient ($\alpha > 10^5$ $cm^{-1}$ in visible and near-infrarred spectral regions) the obtained pyrite thin films have suitable direct bandgap (0.985 eV) for thin film solar cell applications.

ACKNOWLEDGEMENTS
The authors acknowledge FONDECYT-CHILE support (Project N° 1130190). R. Henríquez and P. Leyton acknowledge to the projects FONDEQUIP-CONICYT EQM-140079 and EQM-130170. E.A Dalchiele acknowledge to CSIC (Comisión Sectorial de Investigación Científica) of the Universidad de la República, in Montevideo, Uruguay, PEDECIBA – Física, ANII (Agencia Nacional de Investigación e Innovación) for the partially support.

## References

1. A.G. Pattantyus-Abraham, I.J. Kramer, A.R. Barkhouse, X. Wang, G. Konstantatos, R. Debnath, L. Levian, I. Raabe, M. K. Nazeeruddin, M. Grätzel, E.H. Sargent, *ACS Nano*, 4 (2010) 3374.
2. G. Chen, J. Seo, C. Yang, P.N. Prasad, *Chem. Soc. Rev.*, 42 (2013) 8304.
3. S. Rühle, A.Y. Anderson, H-N. Barad, B. Kupfer, Y. Bouhadana, E. Rosh-Odesh, A. Zaban, *J. Phys. Chem. Lett.*, 3 (2012) 3755.
4. R. W. Miles, G. Zoppi, I. Forbes, *Mater. Today*, 10 (2007) 20.
5. B. Mao, Q. Dong, Z. Xiao, C. L. Exstrom, S. A. Darveau, T. E. Webber, B. D. Lund, H. Huang, Z. Kang, J. Huang, *J. Mater. Chem. A*, 1 (2013) 12060.
6. S.E. Habas, H.A.S. Platt, M.F.A.M. Van Hest, D.S. Ginley, *Chem. Rev.*, 110 (2010) 6571.
7. D. Lincot, *MRS Bulletin*, 35 (2010) 778.
8. C. Wadia, A. P. Alivisatos, D. M. Kammen, *Environ. Sci. Technol.*, 43 (2009) 2072.
9. B. Rezig, h. Dahman, M. Kenzari, *Renew. Energy*, 2 (1992) 125.
10. N. Berry, M. Cheng, C. L. Perkins, M. Limpinsel, J. C. Hemminger, M. Law, *Adv. Energy Mater.*, 2 (2012) 1124.
11. J. Puthussery, S. Seefeld, N. Berry, M. Gibbs, and M. Law, *J. Am. Chem. Soc.*, 133 (2011) 716.
12. D. Spagnoli, K. Refson, K. Wright, and J. D. Gale, *Phys. Rev.* B 81 (2010) 094106.
13. C. Wadia, Y. Wu, S. Gul, S. K. Volkman, J. Guo, A. P. Alivisatos, *Chem. Mater.*, 21 (2009) 2568.
14. R. Sun, M. K. Y. Chan, and G. Ceder, *Phys. Rev., B* 83 (2011) 235311.
15. D. A. Mazón-Montijo, M. T. S. Nair, and P. K. Nair, *ECS J. Solid State Sci. Technol.* 2 (2013) 465.
16. X. Zhang, M. Manno, A. Baruth, M. Johnson, E. S. Aydil, C. Leighton, *ACS Nano*, 7 (2013) 2781.
17. M. Cabán-Acevedo, D. Liang, K. S. Chew, J. P. DeGrave, N. S. Kaiser, S. Jin, *ACS Nano*, 7 (2013) 1731.
18. S. Kment, H. Kmentova, A. Sarkar, R.J. Soukup, N.J. Ianno, D. Sekora, J. Olejnicek, P. Ksirova, J. Krysa, Z. Remes, Z. Hubicka, *Journal of Alloys and Compounds* 607 (2014) 169.
19. S-C Hsiao, C-M Hsu, S-Y Chen, Y-H Perng, Y-L Chueh, L-J Chen, L-H Chou., *Mater. Letter*, 75 (2012) 152.

20. S. Seefeld, M. Limpinsel, Y. Liu, N. Farhi, A. Weber, Y. Zhang, N. Berry, Y. J. Kwon, C. L. Perkins, J. C. Hemminger, R. Wu, M. Law, *J. Am. Chem. Soc.*, 135 (2013) 4412.
21. X Wang, G Wang, J Chen, X Zhu, J Tian, C Jiang, Y. Zhang, X. Liu, R. Wang, *Mater. Lett.*, 110 (2013) 144.
22. A. Gomes, J.R. Ares, I.J. Ferrer, M.I. da Silva, Pereira, C. Sanchez, *Mater. Res. Bull.*, 38 (2003) 1123.
23. Y.Z. Dong, Y.F. Zheng, H. Duan, Y.F. Sun, Y.H. Chen, *Mater. Lett.*, 59 (2005) 2398.
24. [23]. Y.Z. Dong, Y.F. Zheng, X.G. Zhang, H. Duan, Y.F. Sun, Y.H. Chen, *Science in China Series E Technological Sciences*, 48 (2005) 601.
25. S. Nakamura, A. Yamamoto, *Sol. Energy Mater. Sol. Cells*, 65 (2001) 79.
26. X. Qiu, M. Liu, T. Hayashi, M. Miyauchi and K. Hashimoto, *Chem. Commun*., 49 (2013) 1232.
27. D. Lincot, *Thin Solid Films*, 487 (2005) 40.
28. Pau. O. Lupan, T. Pauporté, *J. Cryst. Growth*, 312 (2010) 2454.
29. N. Yu, L. Du, H. Du, Z. Mao, Y. Wang, Y. Wu, D. Liu, *Thin Solid Films*, 550 (2014) 206.
30. A.S.Baranski, W.R. Fawcett, K. Gatner, A.C. McDonald, *J. Electrochem. Soc.*, 130 (1983) 579.
31. D.K. Roe, L. Wenzhao, H. Gerischer, *J. Electroanal. Chem.*, 136 (1982) 323.
32. A.S. Aricò, V. Antonucci, P.L. Antonucci, E. Modica, S. Ferrara, N. Giordano, *Mater. Lett.*, 13 (1992) 12.
33. J. Lambling, R. Bonaterre, G. Cauquis, M. Delamar, G. Demange, *Electrochimica. Acta*, 21 (1976) 119.
34. M. Delamar, J.C. Marchon, *J. Electroanal. Chem.*, 63 (1975) 351.
35. R.P. Martin, W.H. Doubs, J.L. Roberts, D.T. Sawyer, *Inorganic Chem.*, 12 (1973) 1921.
36. B. Margaret, V. Merritt, D.T. Sawyer, *Inorg. Chem.*, 9 (1970) 211.
37. M. Mouanga, P. Bercot, *Int. J. Electrochem. Sci.*, 6 (2011) 1007.
38. N.V. Meurée, *Electrochim. Acta*, 20 (1974) 45.
39. B. Bozzini, E. Griskonis, A. Fanigliulo, A. Sulcius, *Surf. Coat. Technol.*, 154 (2002) 294.
40. [39]. N.S.A. Manan, L. Aldous, Y. Alias, P. Murray, L. J. Yellowlees, M.C. Lagunas, and C. Hardacre, *J. Phys. Chem. B*, 115 (2011) 13873.
41. P. Kush, N.C. Mehra, S. Deka, *Science of Advanced Materials*, 5 (2013) 1.
42. S. Kment, H. Kmentova, A. Sarkar, R.J. Soukup, N.J. Ianno, D. Sekora, J. Olejnicek, P. Ksirova, J. Krysa, R. Remes, Z. Hubicka, *J. Alloys and Compunds*, 607 (2014) 169.
43. B. D. Cullity, Elements of x-ray diffraction, p. xii, Addison-Wesley Pub. Co., Reading, Mass. (1978).
44. J. Pantoja Enríquez, X. Mathew, J. Cryst. Growth., 259 (2003) 215.
45. Yu Bi, Yongbo Yuan, Christopher L. Exstrom, Scott A. Darveau, and Jinsong Huang, *Nano Lett.*, 11 (2011) 4953.
46. A.J. Clayton, S.J.C. Irvine, V. Barrioz, W.S.M. Brooks, G. Zoppi, I. Forbes, K.D. Rogers, D.W. Lane, K. Hutchings, S. Roncallo, *Thin Solid Films* 519 (2011) 7360.
47. R. Yoosuf, M.K. Jayaraj, *Sol Energy Mater Sol Cells*, 89 (2005) 85.
48. R.E. Marotti, C.D. Bojorge, E. Broitman, H.R. Cánepa, J.A. Badán, E.A. Dalchiele, A.J. Gellman, *Thin Solid Films*, 517 (2008) 1077.
49. R. Henríquez, P. Grez, E. Muñoz, H. Gómez, J.A. Badán, R.E. Marotti, E.A. Dalchiele, *Thin Solid Films*, 518 (2010) 1774.
50. S.C. Hsiao, C.M. Hsu, S.Y. Chen, Y.H. Perng, Y,L. Chueh, L.J. Chen, L.H. Chou, *Mater. Letter* 75 (2012) 152.